

A New Formulation of the Spectral Energy Budget of the Atmosphere, With Application to Two High-Resolution General Circulation Models

PIERRE AUGIER,* AND ERIK LINDBORG

Linné Flow Centre, KTH Mechanics, Stockholm, Sweden

Abstract

A new formulation of the spectral energy budget of kinetic and available potential energies of the atmosphere is derived, with spherical harmonics as base functions. Compared to previous formulations, there are three main improvements: (i) the topography is taken into account, (ii) the exact three-dimensional advection terms are considered and (iii) the vertical flux is separated from the energy transfer between different spherical harmonics. Using this formulation, results from two different high resolution GCMs are analyzed: the AFES T639L24 and the ECMWF IFS T1279L91. The spectral fluxes show that the AFES, which reproduces realistic horizontal spectra with a $k^{-5/3}$ inertial range at the mesoscales, simulates a strong downscale energy cascade. In contrast, neither the $k^{-5/3}$ vertically integrated spectra nor the downscale energy cascade are produced by the ECMWF IFS.

1 Introduction

The atmospheric horizontal spectra of velocity components and temperature show a robust $k^{-5/3}$ range at mesoscales (10-500 km) (Nastrom and Gage, 1985). This power law and the corresponding one for the horizontal second order structure functions ($r^{2/3}$) are obtained from signals measured in the troposphere and the stratosphere, over both land and sea (see e.g., Frehlich and Sharman, 2010). It still remains a challenge to reproduce these results in simulations. Some general circulation models (GCMs) (e.g. Koshyk and Hamilton, 2001; Hamilton et al., 2008) and mesoscale numerical weather prediction (NWP) models (Skamarock, 2004) reproduce quite realistic mesoscale spectra. Other GCMs, as for example ECMWF's weather prediction model Integrated Forecast System, produce mesoscale spectra significantly steeper and with smaller magnitude than the measured ones, even with relatively high resolution versions (e.g., Shutts, 2005). The inability of some GCMs to simulate realistic mesoscale spectra must have important consequences in terms of predictability (Vallis, 2006), dispersiveness of ensemble prediction systems (Palmer, 2001) and, evidently, mesoscale NWP.

Even though one can now simulate realistic mesoscale spectra, it is still unclear what physical mechanisms produce them. Theoretically, the only convincing explanation of the $k^{-5/3}$ power law is the hypothesis that it is produced by an (upscale or downscale) energy cascade with a constant energy flux through the scales. Therefore, most of the different theories proposed are based on the hypothesis of an energy cascade: upscale cascade due to 2D-stratified turbulence (Gage, 1979; Lilly, 1983) or downscale cascade due to internal gravity waves (Dewan and Good, 1986; Smith et al., 1987), quasi-

geostrophic dynamics (Tung and Orlando, 2003), surface-quasigeostrophic dynamics (Tulloch and Smith, 2009) or 3D-strongly stratified turbulence (Lindborg, 2006).

The principle of energy conservation strongly constrains the dynamics of the atmosphere. In order to explain the maintenance of the general circulation, Lorenz (1955) developed the concept of available potential energy (APE) and derived an approximate expression proportional to the variance of the temperature fluctuation. His work has laid the foundations for several studies investigating APE (e.g., Boer, 1989; Shepherd, 1993; Siegmund, 1994; Molemaker and McWilliams, 2010) and the atmospheric energy budget through diagnostics of data from global meteorological analysis and GCMs (e.g., Boer and Lambert, 2008; Steinheimer et al., 2008). Due to the multiscale nature of atmospheric motions, spectral analysis can reveal valuable pieces of information from the data (Fjørtoft, 1953) and have therefore become a standard method for diagnostics. However, drawbacks of different used formulations of the spectral energy budget severely limit the results. First of all, the attention has been focused on the budget of kinetic energy (KE) so that in many studies the APE budget is not considered. Most studies investigate only the budget integrated over the total height of the atmosphere and thus the vertical fluxes of energy are not computed. Another very important limitation is that most studies are based on the formulation proposed by Fjørtoft (1953), in which only the purely horizontal and non-divergent flow is considered (e.g., Burrows, 1976; Boer and Shepherd, 1983; Shepherd, 1987; Boer, 1994; Straus and Ditlevsen, 1999; Burgess et al., 2012). This approximation is justified for the very large scales of the atmosphere for which the divergence is indeed very small. However, the approximation may lead to large errors at

* Corresponding author address: Pierre Augier, Linné Flow Centre, KTH Mechanics, Stockholm, Sweden.
E-mail: pierre.augier@mech.kth.se

the mesoscales. Atmospheric measurements show that divergent and rotational spectra are of the same order (Lindborg, 2007) and atmospheric simulations produce divergent spectra of the same order of magnitude as rotational spectra at the mesoscales (e.g., Hamilton et al., 2008; Burgess et al., 2012). Moreover, these results are consistent with theoretical results showing that strongly stratified and weakly rotating flows tend to evolve toward states in which the divergent and rotational components are of the same order of magnitude (Billant and Chomaz, 2001; Lindborg and Brethouwer, 2007). Therefore the spectral energy budget formulations based on the two-dimensional vorticity equation can not capture the dynamics at the mesoscales.

There is no theoretical obstacle in considering the exact three-dimensional advection including both rotational and divergent components of the flow. Lambert (1984) have developed a formulation of the spectral energy budget considering both KE and APE and taking into account the exact advection term. However, the diagnostics was integrated over the total height of the atmosphere so vertical fluxes were not considered. Koshyk and Hamilton (2001) performed a diagnostic of the equation for the KE spectrum (the APE budget was not investigated). The exact advection was computed but the vertical flux was not separated from the energy transfer between spherical harmonics, so it was impossible to define spectral fluxes in a conservative way. Koshyk and Hamilton (2001) separated the spectral pressure term into adiabatic conversion and vertical flux. However, the separation was only approximate. Moreover, as in all previous studies on the spectral energy budget, the topography was neglected. Recently, Brune and Becker (2012) have investigated the effect of the vertical resolution in a mechanistic GCM. Just as in Koshyk and Hamilton (2001), all the terms in the kinetic spectral energy equation were computed at different pressure levels and it was demonstrated that they balance each other. However, spectral fluxes were defined in a non-conservative way and actually also included vertical fluxes.

In order to investigate the energetics of the mesoscales simulated by GCMs, it would be desirable to formulate the spectral energy budget considering both KE and APE, taking the topography into account and making an exact separation of the advection terms into spectral transfer and vertical flux and a corresponding separation of the pressure term into adiabatic conversion, vertical flux and spectral transfer. A formulation meeting these requirements is derived in section 2. In section 3, results from two high resolution GCMs are analyzed.

2 Formulation of the spectral energy budget

2.1 Governing equations in p -coordinates

The analysis is performed in pressure-coordinates in which variables are functions of time, longitude λ , latitude φ (the horizontal coordinates are denoted by \mathbf{x}_h) and pressure. The main advantage of the p -coordinates is that mass conservation can be expressed in the same way as for an in-

compressible fluid: $\nabla \cdot \mathbf{v} = 0$, where $\nabla = (\nabla_h, \partial_p)$ is the gradient operator and $\mathbf{v} = (\mathbf{u}, \omega)$ is the total velocity, with ∇_h the horizontal gradient operator, \mathbf{u} the horizontal velocity and $\omega = D_t p$ the pressure velocity (D_t is the material derivative). The hydrostatic equation is $\partial_p \Phi = -\alpha = -RT/p$, where Φ is the geopotential and α the volume per unit mass.

The potential temperature is given by $\theta = \Lambda(p)T$, with $\Lambda(p) = (p_0/p)^\chi$, $p_0 = 1$ bar, $\chi = R/c_p \simeq 2/7$. For simplicity, the corrections related to the vapor content are neglected. However, the latent heat release is taken into account through the rate of production of internal energy by heating \dot{Q} . The main drawback of the p -coordinates is the complication related to the lower boundary condition (the topography pierces the lower pressure levels). It can be overcome with the formalism developed by Boer (1982) (see appendix) in which the dynamical equations can be written as

$$\partial_t \tilde{\mathbf{u}} = -\mathbf{v} \cdot \nabla \tilde{\mathbf{u}} - f(\varphi) \mathbf{e}_z \wedge \tilde{\mathbf{u}} - \beta \nabla_h \Phi + \beta D_{\mathbf{u}}(\mathbf{u}), \quad (1)$$

$$\partial_t \tilde{\theta}' = -\mathbf{v} \cdot \nabla \tilde{\theta}' - \tilde{\omega} \partial_p \langle \theta \rangle_r + \tilde{Q}_\theta - \beta \partial_t \langle \theta \rangle_r + \beta D_\theta(\theta), \quad (2)$$

where $f(\varphi)$ is the Coriolis parameter, $Q_\theta \equiv \Lambda(p)\dot{Q}/c_p$, $\tilde{\mathbf{u}} = \beta(\mathbf{x}_h, p)\mathbf{u}$, with $\beta(\mathbf{x}_h, p)$ equal to one above the surface and to zero below. The potential temperature fluctuation $\tilde{\theta}'$ is defined as $\tilde{\theta}' = \tilde{\theta} - \beta \langle \theta \rangle_r$, where $\langle \theta \rangle_r = \langle \beta \theta \rangle / \langle \beta \rangle$ is the representative mean, i.e. the mean over regions above the surface (the brackets $\langle \cdot \rangle$ denote the mean over a pressure level). $D_{\mathbf{u}}(\mathbf{u})$ and $D_\theta(\theta)$ are diffusion terms.

2.2 Kinetic and available potential energy forms

Lorenz (1955) showed that the sum of the globally integrated kinetic energy (KE) and available potential energy (APE) is approximately conserved. The mean energies per unit mass are $E_K(p) = \langle |\tilde{\mathbf{u}}|^2 \rangle / 2$ and $E_A(p) = \gamma(p) \langle \tilde{\theta}'^2 \rangle / 2$, with $\gamma(p) = R / (-\Lambda(p)p \partial_p \langle \theta \rangle_r)$. The energy budget can be written as

$$\partial_t E_K(p) = C(p) + \partial_p F_{K\uparrow}(p) - D_K(p), \quad (3)$$

$$\begin{aligned} \partial_t E_A(p) = & G(p) - C(p) + \partial_p F_{A\uparrow}(p) - D_A(p) \\ & + J(p), \end{aligned} \quad (4)$$

where $G(p) = \gamma(p) \langle \tilde{\theta}' \tilde{Q}'_\theta \rangle$ is the forcing by heating (differential heating at very large scales and latent heat release), $C(p) = -\langle \tilde{\omega} \tilde{\alpha} \rangle$ is the conversion of APE to KE, $F_{A\uparrow}(p) = \gamma(p) \langle \omega \tilde{\theta}'^2 \rangle / 2$ and $F_{K\uparrow}(p) = -\langle \omega |\tilde{\mathbf{u}}|^2 \rangle / 2 - \langle \tilde{\omega} \tilde{\Phi} \rangle + \langle \partial_t p_s \Phi_s \beta \rangle$ are the vertical fluxes and $D_K(p)$ and $D_A(p)$ are diffusion terms. The last term of (4), $J(p) = (\partial_p \gamma) \langle \omega \tilde{\theta}'^2 \rangle / 2 - \langle \beta^2 \rangle \langle \omega \rangle_r \langle \alpha \rangle_r$, corresponds to adiabatic processes which do not conserve the Lorenz APE. Siegmund (1994) showed that the globally integrated exact APE and Lorenz APE differ by less than 3%.

2.3 Spectral analysis based on spherical harmonic transform

Each function defined on the sphere can be expanded as a sum of spherical harmonics functions $Y_{lm}(\mathbf{x}_h)$, the normalized eigenfunctions of the horizontal Laplacian operator on the sphere: $|\nabla_h|^2 Y_{lm} = l(l+1)Y_{lm}/a^2$ and $\langle Y_{l'm'}^*, Y_{lm} \rangle = \delta_{ll'} \delta_{mm'}$, where the star denotes the complex conjugate and

l and m are the total and zonal wavenumbers (for details, see Boer, 1983). The velocity is written as

$$\tilde{\mathbf{u}}(\mathbf{x}_h, p) = \sum_{l \geq 0} \sum_{-l \leq m \leq l} \tilde{\mathbf{u}}_{lm}(p) Y_{lm}(\mathbf{x}_h), \quad (5)$$

and the other variables are written in the corresponding way. The spectral KE function $E_K^{[lm]}(p) = |\tilde{\mathbf{u}}_{lm}(p)|^2/2$ is defined so as the mean kinetic energy at a pressure surface is given by $E_K(p) = \sum_{l,m} E_K^{[lm]}(p)$. For APE, the equivalent requirement gives $E_A^{[lm]}(p) = \gamma(p) |\tilde{\theta}'_{lm}(p)|^2/2$.

The spectral energy budget is derived by multiplying equation (1) by $\tilde{\mathbf{u}}_{lm}^*$ and equation (2) by $\gamma(p) \tilde{\theta}'_{lm}$ and then taking the real part of the resulting equations. In order to separate the pressure term into conversion, transfer and vertical flux, we use the continuity equation and the hydrostatic equation to rewrite it as

$$\begin{aligned} -\tilde{\mathbf{u}}_{lm}^* \cdot [\beta \nabla_h \Phi]_{lm} &= -\tilde{\omega}_{lm}^* \tilde{\alpha}_{lm} - \partial_p (\tilde{\omega}_{lm}^* \tilde{\Phi}_{lm}) \\ &\quad - \tilde{\mathbf{u}}_{lm}^* \cdot [\nabla_h \tilde{\Phi}]_{lm} - [\nabla_h \cdot \tilde{\mathbf{u}}]_{lm}^* \tilde{\Phi}_{lm} \\ &\quad - \tilde{\omega}_{lm}^* [\delta \Phi_s]_{lm} - [\partial_t p_s \delta]_{lm}^* \tilde{\Phi}_{lm} \\ &\quad + \tilde{\mathbf{u}}_{lm}^* \cdot [\Phi_s \nabla_h p_s \delta]_{lm}, \end{aligned} \quad (6)$$

In order to separate the advection terms into transfer and vertical flux we rewrite them as

$$\begin{aligned} &-\tilde{\mathbf{u}}_{lm}^* \cdot [\mathbf{v} \cdot \nabla \tilde{\mathbf{u}}]_{lm} = \\ &-\tilde{\mathbf{u}}_{lm}^* \cdot [\mathbf{u} \cdot \nabla_h \tilde{\mathbf{u}}]_{lm} - \tilde{\mathbf{u}}_{lm}^* \cdot [\tilde{\mathbf{u}} \nabla_h \cdot \mathbf{u}]_{lm}/2 \\ &+ ((\partial_p \tilde{\mathbf{u}}_{lm}^*) \cdot [\omega \tilde{\mathbf{u}}]_{lm} - \tilde{\mathbf{u}}_{lm}^* \cdot [\omega \partial_p \tilde{\mathbf{u}}]_{lm})/2 \\ &-\partial_p (\tilde{\mathbf{u}}_{lm}^* \cdot [\omega \tilde{\mathbf{u}}]_{lm})/2, \quad (7) \\ &-\gamma(p) \tilde{\theta}'_{lm} [\mathbf{v} \cdot \nabla \tilde{\theta}']_{lm} = \\ &-\gamma \tilde{\theta}'_{lm} [\mathbf{u} \cdot \nabla_h \tilde{\theta}']_{lm} - \gamma \tilde{\theta}'_{lm} [\tilde{\theta}' \nabla_h \cdot \mathbf{u}]_{lm}/2 \\ &+ \gamma ((\partial_p \tilde{\theta}'_{lm}) [\omega \tilde{\theta}']_{lm} - \tilde{\theta}'_{lm} [\omega \partial_p \tilde{\theta}']_{lm})/2 \\ &-\partial_p (\gamma \tilde{\theta}'_{lm} [\omega \tilde{\theta}']_{lm})/2 \\ &+ (\partial_p \gamma) \tilde{\theta}'_{lm} [\omega \tilde{\theta}']_{lm}/2, \end{aligned} \quad (8)$$

where we have used the continuity equation. Neglecting the non-conservative term in (8) corresponding to the last term in (4), the spectral energy budget can now be written as

$$\begin{aligned} \partial_t E_K^{[lm]}(p) &= C^{[lm]}(p) + T_K^{[lm]}(p) + L^{[lm]}(p) \\ &\quad + \partial_p F_{K\uparrow}^{[lm]}(p) + S_K^{[lm]}(p) - D_K^{[lm]}(p), \end{aligned} \quad (9)$$

$$\begin{aligned} \partial_t E_A^{[lm]}(p) &= G^{[lm]}(p) - C^{[lm]}(p) + T_A^{[lm]}(p) \\ &\quad + \partial_p F_{A\uparrow}^{[lm]}(p) - D_A^{[lm]}(p), \end{aligned} \quad (10)$$

where $T_K^{[lm]}(p)$ and $T_A^{[lm]}(p)$ are spectral transfer terms due to nonlinear interactions, $L^{[lm]}(p)$ is a spectral transfer term arising from the Coriolis and pressure terms, and $S_K^{[lm]}(p)$ is a surface term. Each of the other terms corresponds to a term in (3-4). In contrast to the previous formulations, here, the APE budget is included, the topography is taken into account, the exact three-dimensional advection is considered and the vertical flux terms and the horizontal spectral transfer terms are exactly separated.

The nonlinear KE and APE spectral transfer terms can be expressed as

$$\begin{aligned} T_K^{[lm]}(p) &= \Re \{ -(\tilde{\mathbf{u}}_{lm}^* \cdot [\mathbf{u} \cdot \nabla_h \tilde{\mathbf{u}}]_{lm} + \tilde{\mathbf{u}}_{lm}^* \cdot [\tilde{\mathbf{u}} \nabla_h \cdot \mathbf{u}]_{lm}/2) \\ &\quad + ((\partial_p \tilde{\mathbf{u}}_{lm}^*) \cdot [\omega \tilde{\mathbf{u}}]_{lm} - \tilde{\mathbf{u}}_{lm}^* \cdot [\omega \partial_p \tilde{\mathbf{u}}]_{lm})/2 \}, \end{aligned} \quad (11)$$

$$\begin{aligned} T_A^{[lm]}(p) &= \Re \{ -\gamma (\tilde{\theta}'_{lm} [\mathbf{u} \cdot \nabla_h \tilde{\theta}']_{lm} + \tilde{\theta}'_{lm} [\tilde{\theta}' \nabla_h \cdot \mathbf{u}]_{lm}/2) \\ &\quad + \gamma ((\partial_p \tilde{\theta}'_{lm}) [\omega \tilde{\theta}']_{lm} - \tilde{\theta}'_{lm} [\omega \partial_p \tilde{\theta}']_{lm})/2 \}, \end{aligned} \quad (12)$$

where \Re denotes the real part. The transfer term arising from the Coriolis and pressure terms is

$$\begin{aligned} L^{[lm]}(p) &= \Re \{ -(\tilde{\mathbf{u}}_{lm}^* \cdot [\nabla_h \tilde{\Phi}]_{lm} + [\nabla_h \cdot \tilde{\mathbf{u}}]_{lm}^* \tilde{\Phi}_{lm}) \\ &\quad - \tilde{\mathbf{u}}_{lm}^* \cdot [f(\varphi) \mathbf{e}_z \wedge \tilde{\mathbf{u}}]_{lm} \}. \end{aligned} \quad (13)$$

Each transfer term, as each of the sums of the terms of each line of (11), (12) and (13), is exactly conservative, meaning that it only redistributes energy among the different spherical harmonics at a pressure level. For example, the sum over all spherical harmonics of the first and second lines of (11) are equal to $\langle -\nabla_h(\mathbf{u}|\tilde{\mathbf{u}}|^2) \rangle = 0$ and $\langle (\partial_p \tilde{\mathbf{u}}) \omega \tilde{\mathbf{u}} - \tilde{\mathbf{u}} \omega (\partial_p \tilde{\mathbf{u}}) \rangle = 0$, respectively. The terms in (13) have been gathered together because in plane geometry, where a Fourier decomposition is used, the corresponding terms are zero. Note also that for purely geostrophic motion, these terms cancel each other (except at the surface) and $L^{[lm]}(p) \simeq 0$.

The diabatic term, the conversion term and the diffusion terms are

$$G^{[lm]}(p) = \Re \{ \gamma \tilde{\theta}'_{lm} (\tilde{Q}'_{\theta})_{lm} \}, \quad (14)$$

$$C^{[lm]}(p) = \Re \{ -\tilde{\omega}_{lm}^* \tilde{\alpha}_{lm} \}, \quad (15)$$

$$D_K^{[lm]}(p) = \Re \{ -\tilde{\mathbf{u}}_{lm}^* \cdot [\beta D_{\mathbf{u}}(\mathbf{u})]_{lm} \}, \quad (16)$$

$$D_A^{[lm]}(p) = \Re \{ -\gamma \tilde{\theta}'_{lm} [\beta D_{\theta}(\theta)]_{lm} \}. \quad (17)$$

The vertical fluxes and the surface term are

$$F_{K\uparrow}^{[lm]}(p) = \Re \{ -\tilde{\omega}_{lm}^* \tilde{\Phi}_{lm} - \tilde{\mathbf{u}}_{lm}^* \cdot [\omega \tilde{\mathbf{u}}]_{lm}/2 \}, \quad (18)$$

$$F_{A\uparrow}^{[lm]}(p) = \Re \{ -\gamma \tilde{\theta}'_{lm} [\omega \tilde{\theta}']_{lm}/2 \}, \quad (19)$$

$$\begin{aligned} S_K^{[lm]}(p) &= \Re \{ -\tilde{\omega}_{lm}^* [\Phi_s \delta]_{lm} - [\partial_t p_s \delta]_{lm}^* \tilde{\Phi}_{lm} \\ &\quad + \tilde{\mathbf{u}}_{lm}^* \cdot [\Phi_s \nabla_h p_s \delta]_{lm} \}, \end{aligned} \quad (20)$$

where $\delta = \delta(p_s - p)$ is the Dirac distribution with impulse at the surface (see appendix).

2.4 Vertical integration, summation over zonal wavenumbers and cumulative summation over total wavenumbers

Since the density strongly varies with height in the atmosphere we prefer to include the density when we integrate spectral energies over layers, so that our quantities have the dimension of energy rather than energy per unit mass as in most other studies. With the formulation by Boer, this can be done easily even for pressure levels pierced by the topography. The vertically integrated KE spectrum is defined as

$$E_K[l]_{p_t}^{p_b} = \int_{p_t}^{p_b} \frac{dp}{g} \sum_{-l \leq m \leq l} E_K^{[lm]}(p). \quad (21)$$

The vertically integrated nonlinear spectral flux of kinetic energy is defined as

$$\Pi_K[l]_{p_t}^{p_b} = \sum_{n \geq l} \int_{p_t}^{p_b} \frac{dp}{g} \sum_{-n \leq m \leq n} T_K^{[nm]}(p), \quad (22)$$

and the spectral flux of APE is defined in the corresponding way. When (9) and (10) are vertically integrated, divided by g and summed as in (22) over all the spherical harmonics with total wavenumber $\geq l$, we obtain

$$\begin{aligned} \partial_t \mathcal{E}_K[l]_{p_t}^{p_b} &= \mathcal{C}[l]_{p_t}^{p_b} + \Pi_K[l]_{p_t}^{p_b} + \mathcal{L}[l]_{p_t}^{p_b} \\ &+ \mathcal{F}_{K\uparrow}[l](p_b) - \mathcal{F}_{K\uparrow}[l](p_t) - \mathcal{D}_K[l]_{p_t}^{p_b}, \end{aligned} \quad (23)$$

$$\begin{aligned} \partial_t \mathcal{E}_A[l]_{p_t}^{p_b} &= \mathcal{G}[l]_{p_t}^{p_b} - \mathcal{C}[l]_{p_t}^{p_b} + \Pi_A[l]_{p_t}^{p_b} \\ &+ \mathcal{F}_{A\uparrow}[l](p_b) - \mathcal{F}_{A\uparrow}[l](p_t) - \mathcal{D}_A[l]_{p_t}^{p_b}, \end{aligned} \quad (24)$$

where the terms named $\mathcal{F}_{\uparrow}[l](p) = \sum_{n \geq l} F_{\uparrow}[n]$ are cumulative vertical fluxes and each of the other terms is an integrated cumulation of a corresponding term in (9) and (10). For example, $\mathcal{E}_K[l]_{p_t}^{p_b} = \sum_{n \geq l} E_K[n]_{p_t}^{p_b}$ is the cumulative kinetic energy and $\mathcal{C}_K[l]_{p_t}^{p_b} = \sum_{n \geq l} C[n]_{p_t}^{p_b}$ the cumulative conversion of APE into KE. Putting $l = 0$ in equations (23) and (24) we recover equations (3) and (4) integrated between two pressure surfaces.

3 Application to two GCMs

3.1 Presentation of the data and the models

We have analyzed two data sets produced by two simulations performed with two spectral GCMs: the Atmospheric GCM for the Earth Simulator (AFES) and ECMWF's weather prediction model Integrated Forecast System (IFS). For a precise descriptions of both simulations, see Hamilton et al. (2008) and ECMWF (2010), respectively. The two simulations and the two models are quite different. The AFES is a climate model using a spectral advection scheme. It has been run at high resolution for research purposes. The horizontal resolution is T639, which correspond to a grid space of roughly 20 km. There are 24 vertical levels from the ground to about 1 hPa. Hamilton et al. (2008) showed that the AFES reproduces many features of the atmospheric spectra, especially a realistic $k^{-5/3}$ power law at the mesoscales. ECMWF IFS is a model developed and used for operational deterministic forecast. It uses a semi-Lagrangian advection scheme with a horizontal resolution T1279, which correspond to a grid space of roughly 10 km. There are 91 vertical levels with a minimum pressure of 0.01 Pa. The AFES and the ECMWF simulations correspond to June and December, respectively. We have averaged over 25 days (5 different times) for the ECMWF data set and over 10 days (40 times) for the AFES data set.

The AFES data contain the horizontal velocity, the pressure velocity and the temperature at pressure levels. The geopotential is computed by integrating the hydrostatic relation from the ground. The ECMWF data contain the vorticity, the divergence, the pressure velocity and the temperature at hybrid vertical levels. We compute horizontal velocity and the geopotential and then linearly interpolate the data at pressure levels. Since we do not have access

to the heating rate and to the total dissipative terms, the APE forcing $\mathcal{G}[l]_{p_t}^{p_b}$ and the dissipative terms $\mathcal{D}_K[l]_{p_t}^{p_b}$ and $\mathcal{D}_A[l]_{p_t}^{p_b}$ have not been computed. Since the surface fluxes are modeled in a GCM, we focus on the vertical flux at pressure levels not pierced by the topography. Finally, we have computed the terms $\mathcal{C}[l]_{p_t}^{p_b}$, $\Pi_K[l]_{p_t}^{p_b}$, $\Pi_A[l]_{p_t}^{p_b}$ and $\mathcal{L}[l]_{p_t}^{p_b}$ for all levels and the vertical fluxes $\mathcal{F}_{K\uparrow}[l](p)$ and $\mathcal{F}_{A\uparrow}[l](p)$ for pressure levels not pierced by the topography. The spectral flux arising from the Coriolis and pressure terms $\mathcal{L}[l]_{p_t}^{p_b}$ is completely negligible at wavenumbers $l \gtrsim 30$ consistent with previous computations by Koshyk and Hamilton (2001). At larger scales, it is not negligible at one instant but shows a big randomness in time because it is a sum of large terms which tend to cancel each other. Therefore, one would need to average over long time series to obtain a good statistical convergence. Since our main interest here is the dynamics of the mesoscales and for clarity, this spectral flux is not included in the figures.

3.2 Vertically integrated spectral energy budget

Figure 1(a) presents the globally integrated spectral fluxes and cumulative conversion for the AFES model. By construction the fluxes are equal to zero at $l = l_{\max}$ and should also be equal to zero at $l = 0$, since they represent conservative processes. The total spectral flux (black thick line) is positive at all wavenumbers, which means that in average, the energy is transferred toward large wavenumbers. At leading order, energy is forced at the very large planetary scales and dissipated at smaller scales, and a substantial part is dissipated at the smallest scales simulated.

However, the total spectral flux has a somewhat intricate shape. It reaches a maximum equal to 1.3 W/m² around $l = 4$, decreases to 0.55 W/m² at $l \simeq 20$, increases again to reach a plateau between $l \simeq 70$ and $l \simeq 200$ where $\Pi[l] \simeq 0.82$ W/m² before dropping down to zero at the largest wavenumbers. At $l < 15$, the total flux is largely dominated by the APE spectral flux (blue line), which also increases abruptly around $l = 3$ and decreases abruptly between $l = 6$ and $l = 20$. This indicates that there is a transfer of APE from wavelengths of the order of 10000 km to wavelengths between 2000 km and 5000 km. The strong decrease of $\Pi_A[l]$ is associated with a strong increase of the KE spectral flux (red line) and a strong decrease of the cumulative conversion (dashed dotted line) from $\mathcal{C}[l] = 1.13$ W/m² to $\mathcal{C}[l] = -0.14$ W/m². The variation $\Delta\mathcal{C}[\Delta l]$ of the cumulative conversion over a particular range of wavenumbers Δl represents the energy converted over this range. In this case, the conversion of APE to KE is $\Delta\mathcal{C}[\Delta l] \simeq 1.27$ W/m² over a range of wavelengths between 1000 km to 5000 km. This large conversion at the synoptic scales and the spectral transfer of APE from the planetary scales toward the synoptic scales are mainly due to the baroclinic instability. It is interesting to compare these results with the spectral energy budget of an equilibrated Eady flow (Molemaker and McWilliams, 2010). The general picture is very similar with a dominance of the APE flux at large scales and a stronger KE flux at small scales. The increase of the total nonlinear flux at wavelengths between 700 km to 2000 km indicates that there is a direct forcing of APE

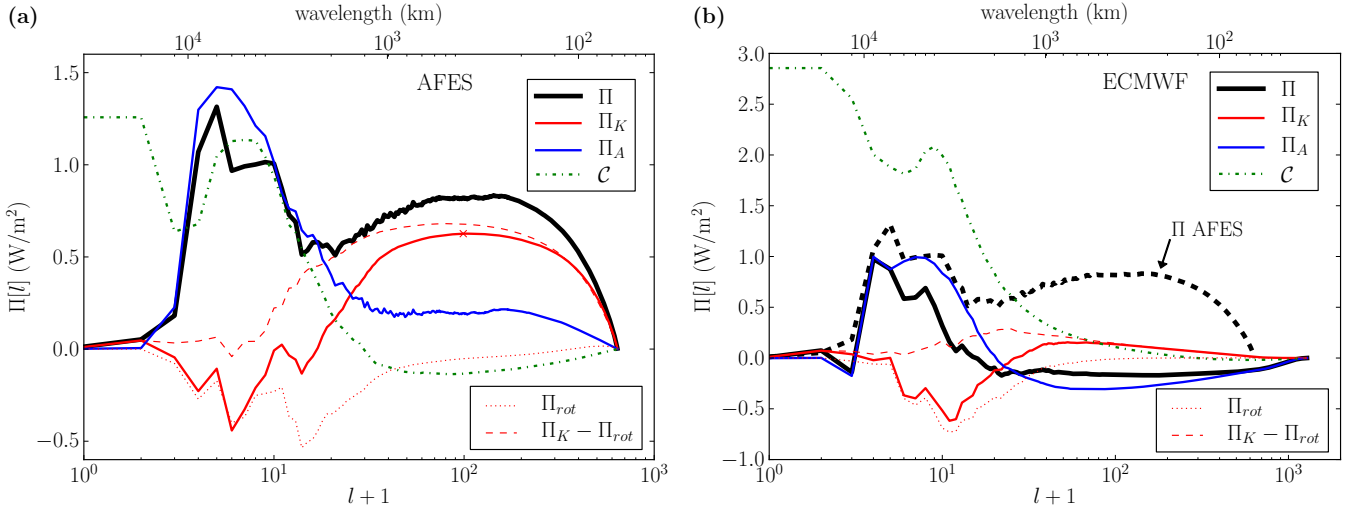


Figure 1: Total, KE and APE nonlinear spectral fluxes and cumulative conversion $\mathcal{C}[l]$ versus total wavenumber for (a) the AFES T639 simulation and (b) the ECMWF IFS T1279 simulation. The cross in (a) marks the maximum value of the KE nonlinear spectral flux $\tilde{\Pi}_K = \max(\Pi_K) = 0.62$ used for nondimensionalization of the spectra in figure 2. In (b), the black dashed line is the spectral flux $\Pi[l]$ for the AFES T639 simulation.

at these scales, most probably due to latent heat release organized at large scales. This interpretation is consistent with results by Hamilton et al. (2008), who reported spectral magnitude at the mesoscales much smaller for the dry dynamical core than for the full AFES.

As already shown, the KE is mainly forced (by a conversion of APE) over a range of wavelengths between 1000 km to 5000 km. At larger scales, the KE spectral flux is negative and reaches a minimum value approximately equal to -0.45 W/m^2 . A portion of the KE is transferred upscale, toward the planetary scales, which feeds the large-scale zonal winds. At smaller scales, the KE spectral flux reaches a plateau at 0.62 W/m^2 . This shows that a non-negligible portion of the KE cascades toward small scales at the mesoscales. The value 0.62 W/m^2 , which after conversion gives $6.1 \times 10^{-5} \text{ m}^2/\text{s}^3$, is consistent with previous estimations for the KE spectral flux and for the small-scale dissipation rate (Cho and Lindborg, 2001). Remarkably, the cumulative conversion $\mathcal{C}[l]$ increases at the mesoscales (the local conversion is negative), showing that the conversion is from KE to APE. This demonstrates that the KE $k^{-5/3}$ spectrum is not produced by direct forcing of the KE. Note that this conversion from KE to APE is consistent with strongly stratified turbulence.

One should not interpret the wavenumber where $\Pi_K[l]$ changes sign as the wavenumber where both upscale and downscale fluxes start. These two processes actually coexist in the same range of scales. The nonlinear KE spectral flux computed only with the rotational flow, Π_{rot} , is plotted as a red dotted line. The interactions between the rotational modes conserve both KE and enstrophy ($|\nabla_h \wedge \mathbf{u}|^2/2$), exactly as in two-dimensional turbulence. Note that Π_{rot} is the spectral flux computed when the framework based on the two-dimensional vorticity equation is adopted, as for example in Boer and Shepherd (1983). We see that these interactions are responsible for the upscale flux, which actually starts at wavelengths of the order of 1800 km.

In contrast, the complementary flux, $\Pi_K[l] - \Pi_{rot}$, (red dashed line) is responsible for the downscale energy flux which starts at wavelengths of the order of 2000 km. Indeed, the downscale energy cascade is produced by interactions involving the divergent part of the velocity field (Molemaker et al., 2010; Deusebio et al., 2012).

As shown by Lambert (1984), the variations of the cumulative conversion at very small wavenumber $l < 8$ are due to the Hadley and Ferrel circulations. The decrease of $\mathcal{C}[l]$ at $l = 2$ corresponding to a conversion of APE to KE of approximately 0.6 W/m^2 is mainly the signature of the Hadley cell. The increase of $\mathcal{C}[l]$ at $l = 4$ corresponding to a conversion of KE to APE of approximately 0.5 W/m^2 is mainly the signature of the Ferrel cell. The conversion at $l = 2$ is weaker than previously computed by Lambert (1984). Further investigations are necessary to understand if this effect is due to averaging over an insufficient amount of data or if it is a robust aspect of the AFES.

Figure 1(b) presents the globally integrated spectral fluxes and cumulative conversion as in figure 1(a) but for the ECMWF model. The large-scale features are overall quite similar to the results for the other model even though the conversion at wavenumbers smaller than 4 corresponding to the Hadley cell is much stronger ($\Delta\mathcal{C}[\Delta l] \simeq 1 \text{ W/m}^2$). The baroclinic instability leads to large-scale positive APE flux and strong conversion at the synoptic scales $\Delta\mathcal{C}[\Delta l] \simeq 1.5 \text{ W/m}^2$. However, the KE flux increases much less than for the AFES, indicating that there is strong dissipation at wavelengths of the order of 1000 km. The total spectral flux for the AFES is also plotted in dashed black line for comparison. The total flux for the ECMWF model is slightly smaller than for the AFES at the synoptic scales and is negative and very small at the mesoscales. This is related to the weakness of the downscale mesoscale KE cascade ($\Pi_K[l] \simeq 0.15 \text{ W/m}^2$) and to the fact that the APE flux is negative ($\Pi_A[l] \simeq -0.3 \text{ W/m}^2$). This unexpected result could be due to direct forcing of APE by release of

latent heat at the smallest resolved scales of the order of 50 km. This interpretation is consistent with the sign of the local conversion at the mesoscales, from APE to KE, in contrast to the case of the AFES.

3.3 Vertically integrated non-dimensional spectra

If it is assumed that the $l^{-5/3}$ range of the kinetic energy spectrum is of a similar form as the Kolmogorov spectrum of isotropic turbulence, then $E_K \propto \Pi_K^{2/3} l^{-5/3}$. If it is further assumed that the only other parameters that determine the spectrum are the Earth's radius, a , and the total mass per unit area, which is equal to $\langle p_s \rangle / g$, then dimensional considerations give

$$E_K[l] = C(\langle p_s \rangle / g)^{1/3} (a \Pi_K)^{2/3} l^{-5/3}, \quad (25)$$

where C is a constant supposedly of the order of unity. In the following, we choose as the typical KE flux the maximum of the KE flux in the mesoscales: $\tilde{\Pi}_K = \max(\Pi_K) = 0.62$. (This value is marked by a cross in figure 1a.) In figure 2(a) the non-dimensional compensated spectra $E[l] l^{5/3} (\langle p_s \rangle / g)^{-1/3} (a \tilde{\Pi}_K)^{-2/3}$ for the AFES model are plotted as a function of the total wavenumber. At $l = 1$, the APE spectrum (blue line) is much larger than the KE spectrum (red line), as predicted by Lorenz (1955). This leads to a ratio mean APE over mean KE approximately equal to 3. However, for other wavenumbers (except at the largest ones), both spectra are of the same order of magnitude. At the synoptic scales, the KE spectrum is quite steep. It shallows at the mesoscales and presents a flat plateau corresponding to a $l^{-5/3}$ inertial range from 650 km up to the large-wavenumber dissipative range. Remarkably, the constant C in equation (25) is very close to unity, which indicates that the $l^{-5/3}$ mesoscale range may be explained in a similar way as Kolmogorov (1941) explained the $k^{-5/3}$ range of isotropic turbulence. At wavelengths between 700 km to 2000 km, the APE spectrum (blue line) is equal to or larger than the KE spectrum and there are fluctuations resembling noise. However, the fluctuations do not seem related to lack of statistics. They could be due to the direct forcing of APE at this scales (see figure 1a).

In figure 2 are also plotted the rotational spectrum $E_{rot}[l]$ and the divergent spectrum $E_{div}[l]$. In order to define these spectra, one has to consider an alternative expansion of the velocity field than in (5),

$$\mathbf{u} = \sum_{l \geq 0} \sum_{-l \leq m \leq l} \psi_{lm} \mathbf{Y}_{lm}^{(rot)}(\mathbf{x}_h) + \chi_{lm} \mathbf{Y}_{lm}^{(div)}(\mathbf{x}_h), \quad (26)$$

where $\mathbf{Y}_{lm}^{(rot)} = a \mathbf{e}_z \wedge \nabla_h Y_{lm}$ and $\mathbf{Y}_{lm}^{(div)} = a \nabla_h Y_{lm}$ are the vector spherical harmonics satisfying the orthogonal condition $\langle \mathbf{Y}_{lm}^{(\alpha)} | \mathbf{Y}_{l'm'}^{(\alpha')} \rangle = l(l+1) \delta_{\alpha\alpha'} \delta_{ll'} \delta_{mm'}$. The spherical stream function $\psi(\mathbf{x}_h, p)$ is related to the vertical component of the vorticity by $\zeta \equiv \mathbf{e}_z \cdot (\nabla_h \wedge \mathbf{u}) = -a |\nabla_h|^2 \psi$ and the spherical velocity potential $\chi(\mathbf{x}_h, p)$ is related to the horizontal divergence by $d \equiv \nabla_h \cdot \mathbf{u} = a |\nabla_h|^2 \chi$. We see that the divergent and rotational spectra can be defined as

$$E_{div}[l] = \sum_{-l \leq m \leq l} \frac{a^2 |d_{lm}|^2}{2l(l+1)}, \quad E_{rot}[l] = \sum_{-l \leq m \leq l} \frac{a^2 |\zeta_{lm}|^2}{2l(l+1)}.$$

With these definitions, $\sum_{l \geq 0} E_{div}[l] + E_{rot}[l]$ is equal to the total energy although $E_{div}[l] + E_{rot}[l]$ is not exactly equal to the KE spectrum (Koshyk and Hamilton, 2001). At large scales, the rotational spectrum $E_{rot}[l]$ (dashed red line) largely dominates over the divergent spectrum $E_{div}[l]$ (dashed dotted red line). Remarkably, the compensated divergence spectrum increases with l , meaning that $E_{div}[l]$ is shallower than a $l^{-5/3}$ power law. Such very shallow divergent spectra were also obtained by simulations of strongly stratified and strongly rotating turbulence forced in geostrophic modes (Deusebio et al., 2012) and of strongly stratified turbulence forced with rotational modes (Augier et al., 2012). However, other simulations with higher resolution would be necessary in order to check whether the divergent spectra are sensitive to model parametrizations and resolution. At the mesoscales, both spectra are of the same order of magnitude even though $E_{rot}[l]$ is still larger than $E_{div}[l]$.

Figure 2(b) shows the non-dimensional compensated spectra for the ECMWF model (we use the same value as for the AFES of $\tilde{\Pi}_K$ in order to allow a easier comparison between both models). The large-scale features are very similar to the AFES. At the synoptic scales, the ratio $E_K[l]/E_A[l]$ is approximately equal to 2, indicating that the energy is partitioned equally between the two components of KE and the APE, as predicted by Charney (1971). In contrast to the KE spectrum, the APE spectrum becomes more shallow at high wavenumbers. This is probably related to direct forcing of APE at the mesoscales. Interestingly, the compensated divergent spectrum is flat, which means that it follows a $l^{-5/3}$ power law. However, its magnitude is very small so that the vertically integrated KE spectrum at the mesoscales is nearly not affected. It is interesting to note the similarity with the $k^{-5/3}$ divergent spectra obtained by Waite and Snyder (2009) simulating a baroclinic life cycle.

3.4 Vertical decomposition and vertical energy fluxes

Figure 3 presents the spectral fluxes and the cumulative conversion integrated over two different layers corresponding approximately to the upper troposphere (a,b) and the stratosphere (c,d). Figures (a,c) correspond to the AFES T639 simulation and figures (b,d) to the ECMWF IFS T1279 simulation. Figure 3 also presents the cumulative total vertical fluxes, $\mathcal{F}_\uparrow[l](p_b)$, at the bottom, and $\mathcal{F}_\uparrow[l](p_t)$, at the top of the layer (magenta dashed and dashed-dotted lines, respectively). The balance between these two inward and outward terms, $\Delta_{p_t}^{p_b} \mathcal{F}_\uparrow[l] = \mathcal{F}_\uparrow[l](p_b) - \mathcal{F}_\uparrow[l](p_t)$, is plotted in magenta as a continuous line.

For the AFES simulation, the spectral fluxes and the cumulative conversion integrated over the upper troposphere (figure 3a) present roughly the same features as the globally integrated terms shown in figure 1(a). The KE flux in the upper troposphere accounts for approximately one third of the globally integrated KE spectral flux. The cumulative vertical flux $\Delta_{p_t}^{p_b} \mathcal{F}_\uparrow[l]$ is relatively small at the mesoscales and at the synoptic scales, indicating that at leading order, the energy budget in this layer and at these scales is dominated by the spectral fluxes rather than by

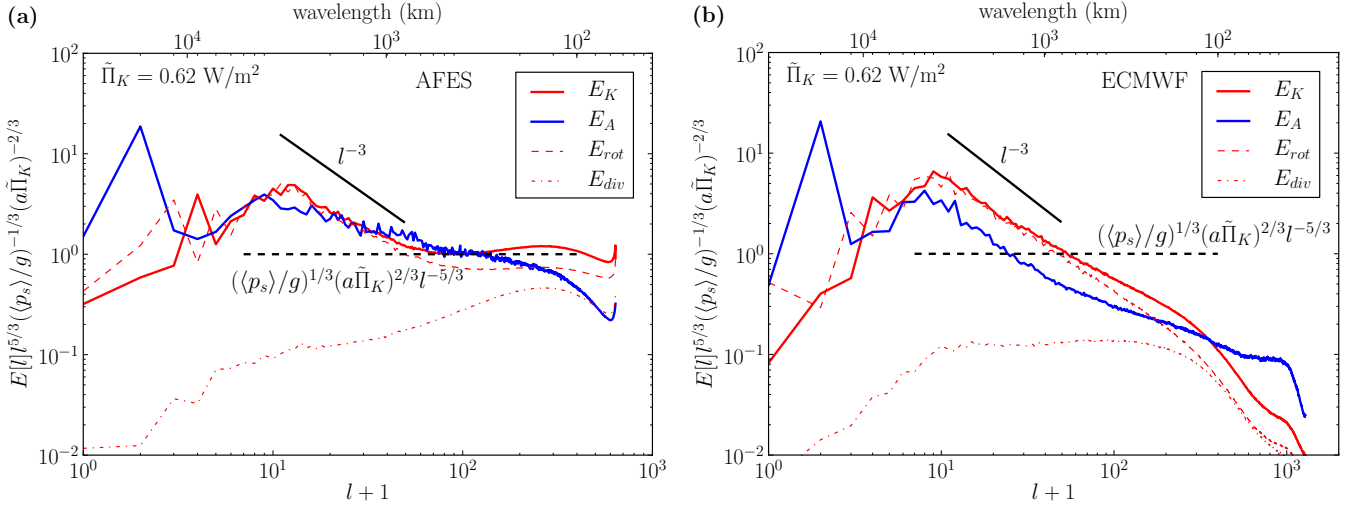


Figure 2: Non-dimensional compensated spectra versus total wavenumber for (a) the AFES T639 simulation and (b) the ECMWF IFS T1279 simulation. The black dashed line represents the prediction (25) with $\tilde{\Pi}_K = 0.62$ (value marked by a cross in figure 1a). The continuous straight line indicates the l^{-3} power law.

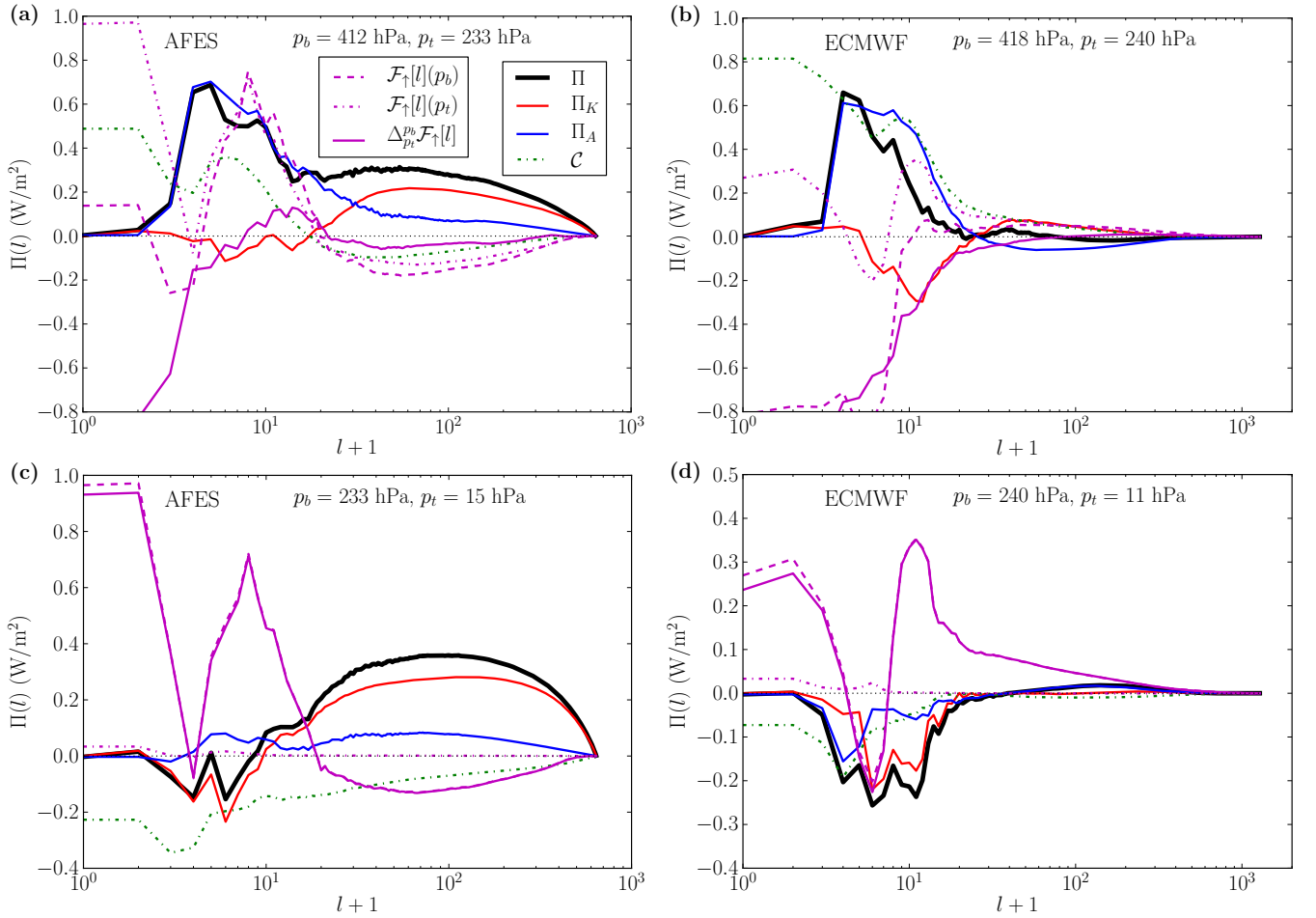


Figure 3: Same as figures 1 but integrated over layers corresponding approximately to (a,b) the stratosphere and (c,d) the upper troposphere. Figures (a,c) correspond to the AFES T639 simulation and figures (b,d) to the ECMWF IFS T1279 simulation. The legend is given in (a) and $\Delta_{p_t}^{p_b} \mathcal{F}_\uparrow[l] = \mathcal{F}_\uparrow[l](p_b) - \mathcal{F}_\uparrow[l](p_t)$ is the cumulative inward vertical flux.

the vertical fluxes. However, at the top and the bottom of the layer, there are large vertical fluxes which are approximately equal. These fluxes through the upper troposphere (upward at wavenumbers $7 \leq l \leq 20$ and downward at wavenumbers $3 \leq l \leq 6$) account for exchanges of energy between the lower troposphere and the stratosphere. At wavenumbers $1 \leq l \leq 2$, $\mathcal{F}_\uparrow[l](p_t)$ decreases from 1 W/m^2 to 0 W/m^2 indicating a strong upward vertical flux at $p_t = 233 \text{ hPa}$. Since the vertical flux at the bottom layer is small at these wavenumbers, the layer loses energy. The wavenumber ranges of the upward and downward fluxes at the planetary scales nearly coincide with the wavenumber ranges of the conversion due to the Hadley and Ferrel cells, which seems to indicate that these vertical fluxes are related to the large-scale cells. In contrast, the upward flux at the synoptic scales indicates the presence of upward propagating planetary waves. At $l > 70$, $\mathcal{F}_\uparrow[l](p_b)$ and $\mathcal{F}_\uparrow[l](p_t)$ increase meaning that there are downward vertical fluxes. This shows that in the AFES, the mesoscales of the upper troposphere are not directly forced by upward propagating gravity waves, as was the case in the simulation by Koshyk and Hamilton (2001) using the SKYHI model.

Figure 3(b) presents the same quantities as figure 3(a), also integrated over the upper troposphere but for the ECMWF model. Comparing figures 3(a) and 3(b), we see the same differences as we saw between figures 1(a) and 1(b). The vertical fluxes are also quite different from the AFES with small upward fluxes at the mesoscales and a smaller magnitude of the variations of the cumulative fluxes at large scales.

Figure 3(c) shows the same quantities as figure 3(a), also for the AFES but integrated over the stratosphere. At the large scales, the spectral fluxes and the cumulative conversion are quite different from the terms integrated over the height of the atmosphere and over the upper troposphere. The APE flux has no large peak at $l \simeq 4$ and there is a conversion from KE to APE at synoptic scales rather than the other way around, as in the upper troposphere. On the other hand, there is a strong upward energy flux at large scales from the bottom layer at $p_b = 233 \text{ hPa}$ while the corresponding flux at the top layer at $p_t = 15 \text{ hPa}$ is very small. Thus, the stratosphere is not directly forced by baroclinic instability but by an energy flux from the troposphere, due to upwards propagating planetary waves and possibly also the effects of the Hadley and the Ferrel cells (see figure 3a). At the mesoscales, there is a conversion of KE into APE and a strong downscale cascade of KE and APE accounting for approximately half the globally integrated flux. At $l > 80$, $\Delta_{p_t}^{p_b} \mathcal{F}_\uparrow[l] \simeq \mathcal{F}_\uparrow[l](p_b)$ increases, meaning that the stratosphere loses energy by a downward flux through the tropopause.

Figure 3(d) presents the same quantities as figure 3(c), also integrated over the stratosphere but for the ECMWF model. Note that the vertical axis is different from figure 3(c). In contrast to the AFES, there is nearly no downscale energy cascade and the stratospheric mesoscales are directly forced by an upward energy flux.

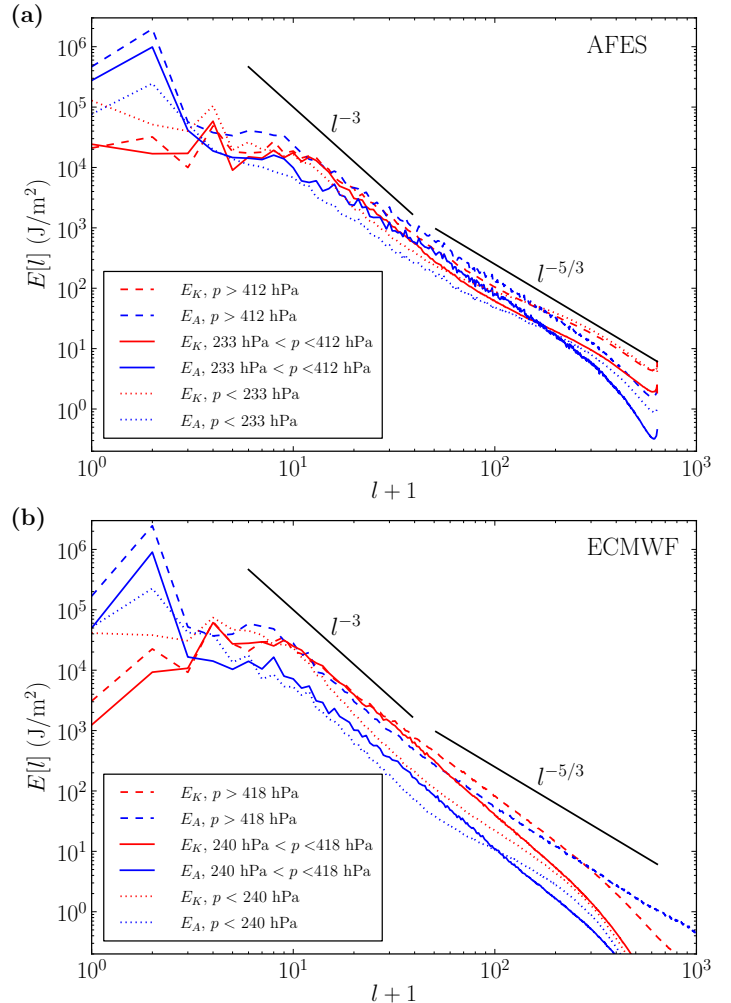


Figure 4: KE and APE spectra integrated over three layers corresponding approximately to the lower troposphere, the upper troposphere and the upper atmosphere. The straight black lines indicate the l^{-3} and $l^{-5/3}$ dependencies as guides for the eye. Note that the axes and the straight lines are exactly the same in (a) and (b).

Figure 4 presents the KE and APE spectra integrated over three layers corresponding approximately to the lower troposphere, the upper troposphere and the upper atmosphere, for the AFES (figure 4a) and the ECMWF model (figure 4b). Note that the axes and the straight lines are exactly the same in both figures. At the large scales the spectra for both models are similar but at the mesoscales the spectral magnitude of the ECMWF is much smaller than the magnitude of the AFES. Spectra integrated over the different layers lie closer to each other for the AFES than for the ECMWF. For the AFES the KE spectra have similar shapes at different layers, whereas for the ECMWF model, they are quite different with a shallowing at the mesoscales only in the stratosphere (blue and red dotted lines) as reported by Burgess et al. (2012). However, these shallow spectra are much smaller in magnitude than the corresponding spectra from the AFES model (more than one order of magnitude smaller at $l \simeq 100$). From figure 3(d) it is quite clear that the shallowing of the stratospheric spectra of the ECMWF model is not caused by

an energy cascade but rather by gravity waves propagating from the troposphere. The integrated spectra of the ECMWF model (figure 2b) is dominated by the contribution from the troposphere. In the lower troposphere, the APE spectrum presents a $l^{-5/3}$ dependency and is larger than the KE spectrum at large wavenumbers. However, this cannot be explained by a downscale energy cascade since the APE spectral flux is small and negative. These differences between the APE and the KE spectra could be due to a damping of the KE and to a direct diabatic forcing of the APE at the very large wavenumbers $l \sim 1000$. For the AFES model (figure 4a), the spiky irregular shape observed at the synoptic scales for the globally integrated APE spectrum (figure 2a) is also observed for the tropospheric APE spectra but not for the stratospheric APE spectrum. This could indicate that this effect is related to the topography. However, the spikes are not only present in the lower but also in the upper tropospheric spectra whereas the upper troposphere is not pierced by the topography. Moreover, the vertical fluxes at $p = 412$ hPa are rather regular. Therefore, the spiky irregular shape of the APE spectra seems to be due to processes happening in the troposphere and not only at the surface. The release of latent heat organized at the synoptic scales could be an explanation.

4 Conclusions

A new formulation of the spectral energy budget has been presented and applied to study the results of two different GCMs. In contrast to previous formulations, both KE and APE are considered and the topography is taken into account. Moreover, the advection terms are exactly separated into spectral transfer and vertical flux and the pressure term is exactly separated into adiabatic conversion, vertical flux and spectral transfer.

The spectral fluxes show that the AFES, which reproduces realistic spectra with a $k^{-5/3}$ power law at the mesoscales, simulates a strong downscale energy cascade of $\Pi[l] \simeq 0.8$ W/m². The vertical fluxes for the upper troposphere show that the mesoscales are not directly energized by gravity waves propagating from the ground. Moreover, the spectra collapse on the prediction based on the existence of the cascade, indicating that the mesoscale $k^{-5/3}$ power law is due to the downscale energy cascade. In contrast, neither the $k^{-5/3}$ spectra nor the downscale energy cascade are produced by the ECMWF model. The study of the spectra and their tendencies integrated over different layers reveals that in the AFES, the stratospheric mesoscales are not forced by upward propagating gravity waves. In contrast to this, the stratospheric spectra of the ECMWF model are directly forced at the mesoscales by gravity waves propagating from the troposphere.

These results show that our spectral energy budget formulation is a convenient tool to investigate the issue of the mesoscale dynamics and its simulation by GCMs. In particular, we have shown that the flux computed only with the rotational part of the velocity field Π_{rot} (as i.e. in Fjørtoft, 1953; Boer and Shepherd, 1983) accounts only for the upscale KE flux. Since the downscale energy cascade is produced by interactions involving the divergent part of the

velocity field (Vallgren et al., 2011; Deusebio et al., 2012; Molemaker et al., 2010), one must consider the nonlinear transfers computed with the total advection term. To do this in a consistent way, the pressure term and the advection terms in the spectral energy budget have to be decomposed as shown in section 2.

Future investigations could compare different models varying the resolution, the convection schemes, the advection scheme and the turbulent models. It would be desirable to analyze simulations over long periods to obtain better statistical convergence at large scales. In particular, this would be necessary in order to obtain statistical convergence of the linear term (13) at large scales. Moreover, it could be informative to analyze idealized simulations using dry dynamical core and/or aquaplanet versions of the models with variation of physical parameters such as the rotation rate and the large-scale forcing. Other interesting aspects for future work are the consideration of the effects of the water content and the adaptation of the formulation for non-hydrostatic simulations.

We wish to thank Kevin Hamilton and Nils Wedi for providing the data. We also thank Kevin Hamilton for showing nice hospitality in Hawaii and Nathanael Schaeffer for providing his library for spherical harmonic transform SHTns (Schaeffer, 2012).

Technical details on topography in p -coordinates

Following Boer (1982), the equations are extended over a domain including subterranean pressure levels. For any function $f(\mathbf{x}_h, p)$ whose values below the surface have been obtained by interpolation, we define a corresponding function $\tilde{f}(\mathbf{x}_h, p) = \beta(\mathbf{x}_h, p)f(\mathbf{x}_h, p)$, where $\beta(\mathbf{x}_h, p) = H(p_s(\mathbf{x}_h) - p)$ and H is the Heaviside function. In the extended domain, the boundary condition at the earth surface is expressed as $D_t\beta = 0$, with $D_t = \partial_t + \mathbf{v} \cdot \nabla$. Using the chain rules $\partial_t\beta = \delta\partial_t p_s$, $\nabla_h\beta = \delta\nabla_h p_s$, $\partial_p\beta = -\delta$, we recover the classical boundary condition for the atmospheric domain in pressure coordinates: $D_t\beta = \delta(\partial_t p_s + \mathbf{u} \cdot \nabla_h p_s - \omega_s) = 0$, where $\delta = \delta(p_s - p)$ is the Dirac distribution with impulse at the surface.

In practice, computing the spherical harmonics transform of $\tilde{\mathbf{u}} = \beta\mathbf{u}$ is not numerically feasible at pressure levels pierced by the topography, i.e. where β is equal both to 1 and to 0. We must use a modified smooth β . Moreover, the spherical harmonic transform of $\tilde{\mathbf{u}} = \beta\mathbf{u}$ should not reflect the spectral content of the topography rather than that of \mathbf{u} . Therefore, it is convenient to use an alternative β computed with a time-averaged pressure surface $\overline{p_s}(\mathbf{x}_h)$ (Boer, 1982). A smooth low-pass filter with a cutoff total wavenumber equal to 40 is then applied to this function $H(\overline{p_s}(\mathbf{x}_h) - p)$. In this way, a large part of the interpolated subterranean data (mainly under the large topographic highs, i.e. Antarctic continent, Himalaya and

Andean mountain ranges) are not used in the calculations, but the spectral quantities at relatively high wavenumbers are not affected by the high wavenumber content of the topography.

References

- Augier, P., P. Billant, and J.-M. Chomaz, 2012: Stratified turbulence forced with columnar dipoles. Part 2. Numerical study. *submitted to J. Fluid Mech.*
- Billant, P. and J.-M. Chomaz, 2001: Self-similarity of strongly stratified inviscid flows. *Phys. Fluids*, **13**, 1645–1651.
- Boer, G. and S. Lambert, 2008: The energy cycle in atmospheric models. *Clim. Dyn.*, **30**, 371–390.
- Boer, G. J., 1982: Diagnostic equations in isobaric coordinates. *Monthly weather review*, **110**, 1801–1820.
- Boer, G. J., 1983: Homogeneous and Isotropic Turbulence on the Sphere. *J. Atmos. Sci.*, **40**, 154–163.
- Boer, G. J., 1989: On exact and approximate energy equations in pressure coordinates. *Tellus*, **41**, 97–108.
- Boer, G. J., 1994: Mean and Transient Spectral Energy and Enstrophy Budgets. *J. Atmos. Sci.*, **51** (13), 1765–1779.
- Boer, G. J. and T. G. Shepherd, 1983: Large-Scale Two-Dimensional Turbulence in the Atmosphere. *J. Atmos. Sci.*, **40**, 164–184.
- Brune, S. and E. Becker, 2012: Indications of stratified turbulence in a mechanistic GCM. *J. Atmos. Sci.*
- Burgess, A., A. Erler, and T. Shepherd, 2012: The Troposphere-to-Stratosphere Transition in Kinetic Energy Spectra and Nonlinear Spectral Fluxes as Seen in ECMWF Analyses. *J. Atmos. Sci.*
- Burrows, W., 1976: Diagnostic Study of Atmospheric Spectral Kinetic Energetics. *J. Atmos. Sci.*, **33** (12), 2308–2321.
- Charney, J. G., 1971: Geostrophic Turbulence. *J. Atmos. Sci.*, **28** (6), 1087–&.
- Cho, J. Y. N. and E. Lindborg, 2001: Horizontal velocity structure functions in the upper troposphere and lower stratosphere 1. Observations. *J. Geoph. Res.-Atmos.*, **106** (D10), 10223–10232.
- Deusebio, E., A. Vallgren, and E. Lindborg, 2012: Rossby and Froude number dependence in geostrophic turbulence. *Submitted to J. Fluid Mech.*
- Dewan, E. M. and R. E. Good, 1986: Saturation and the universal spectrum for vertical profiles of horizontal scalar winds in the atmosphere. *J. Geophys. Res.-Atmos.*, **91** (D2), 2742–2748.
- ECMWF, 2010: IFS documentation, version CY36r1. <http://www.ecmwf.int/research/ifsdocs>.
- Fjørtoft, R., 1953: On the Changes in the Spectral Distribution of Kinetic Energy for Twodimensional, Nondivergent Flow. *Tellus*, **5** (3), 225–230.
- Frehlich, R. and R. Sharman, 2010: Climatology of Velocity and Temperature Turbulence Statistics Determined from Rawinsonde and ACARS/AMDAR Data. *J. Appl. Meteor. Climatol.*, **49**, 1149–1169.
- Gage, K. S., 1979: Evidence for a $k^{-5/3}$ Law Inertial Range in Mesoscale Two-Dimensional Turbulence. *J. Atmos. Sci.*, **36** (10), 1950–1954.
- Hamilton, K., Y. O. Takahashi, and W. Ohfuchi, 2008: Mesoscale spectrum of atmospheric motions investigated in a very fine resolution global general circulation model. *J. Geophys. Res.-Atmos.*, **113** (D18).
- Kolmogorov, A. N., 1941: The local structure of turbulence in incompressible viscous fluids for very large reynolds numbers. *Compt. Rend. Acad. Sci. (USSR)*, **30**, 301–305.
- Koshyk, J. N. and K. Hamilton, 2001: The Horizontal Kinetic Energy Spectrum and Spectral Budget Simulated by a High-Resolution Troposphere-Stratosphere-Mesosphere GCM. *J. Atmos. Sci.*, **58** (4), 329–348.
- Lambert, S., 1984: A global available potential energy-kinetic energy budget in terms of the two-dimensional wavenumber for the FGGE year. *Atmos.-Ocean*, **22**, 265–282.
- Lilly, D. K., 1983: Stratified Turbulence and the Mesoscale Variability of the Atmosphere. *J. Atmos. Sci.*, **40**, 749–761.
- Lindborg, E., 2006: The energy cascade in a strongly stratified fluid. *J. Fluid Mech.*, **550**, 207–242.
- Lindborg, E., 2007: Horizontal Wavenumber Spectra of Vertical Vorticity and Horizontal Divergence in the Upper Troposphere and Lower Stratosphere. *J. Atmos. Sci.*, **64** (3), 1017–1025.
- Lindborg, E. and G. Brethouwer, 2007: Stratified turbulence forced in rotational and divergent modes. *J. Fluid Mech.*, **586**, 83–108.
- Lorenz, E. N., 1955: Available potential energy and the maintenance of the general circulation. *Tellus*, **7**, 157.
- Molemaker, M. J. and J. C. McWilliams, 2010: Local balance and cross-scale flux of available potential energy. *J. Fluid Mech.*, **645**, 295–314.
- Molemaker, M. J., J. C. McWilliams, and X. Capet, 2010: Balanced and unbalanced routes to dissipation in an equilibrated Eady flow. *J. Fluid Mech.*, **654**, 35–63.
- Nastrom, G. D. and K. S. Gage, 1985: A climatology of atmospheric wavenumber spectra of wind and temperature observed by commercial aircraft. *J. Atmos. Sci.*, **42** (9), 950–960.

- Palmer, T., 2001: A nonlinear dynamical perspective on model error: A proposal for non-local stochastic-dynamic parametrization in weather and climate prediction models. *Q. J. R. Meteorol. Soc.*, **127** (572, Part b), 279–304.
- Schaeffer, N., 2012: Efficient Spherical Harmonic Transforms aimed at pseudo-spectral numerical simulations. *ArXiv*.
- Shepherd, T., 1987: A Spectral View of Nonlinear Fluxes and Stationary Transient Interaction in the Atmosphere. *J. Atmos. Sci.*, **44** (8), 1166–1178.
- Shepherd, T. G., 1993: A Unified Theory of Available Potential Energy. *Atmos.-Ocean*, **31** (1), 1–26.
- Shutts, G., 2005: A kinetic energy backscatter algorithm for use in ensemble prediction systems. *Q. J. R. Meteorol. Soc.*, **131** (612), 3079–3102.
- Siegmund, P., 1994: The generation of available potential energy, according to Lorenz' exact and approximate equations. *Tellus*, **46** A, 566–582.
- Skamarock, W. C., 2004: Evaluating mesoscale NWP models using kinetic energy spectra. *Mon. Weather Rev.*, **132** (12), 3019–3032.
- Smith, S. A., D. C. Fritts, and T. E. Vanzandt, 1987: Evidence for a Saturated Spectrum of Atmospheric Gravity-Waves. *J. Atmos. Sci.*, **44** (10), 1404–1410.
- Steinheimer, M., M. Hantel, and P. Bechtold, 2008: Convection in Lorenz's global energy cycle with the ECMWF model. *Tellus A*, **60**, 1001–1022.
- Straus, D. and P. Ditlevsen, 1999: Two-dimensional turbulence properties of the ECMWF reanalyses. *Tellus Ser. A-Dyn. Meteorol. Oceanol.*, **51** (5), 749–772.
- Tulloch, R. and K. S. Smith, 2009: Quasigeostrophic Turbulence with Explicit Surface Dynamics: Application to the Atmospheric Energy Spectrum. *J. Atmos. Sci.*, **66**, 450–467.
- Tung, K. K. and W. W. Orlando, 2003: The k^{-3} and $k^{-5/3}$ Energy Spectrum of Atmospheric Turbulence: Quasigeostrophic Two-Level Model Simulation. *J. Atmos. Sci.*, **60** (6), 824–835.
- Vallgren, A., E. Deusebio, and E. Lindborg, 2011: Possible Explanation of the Atmospheric Kinetic and Potential Energy Spectra. *Phys. Rev. Lett.*, **107** (26).
- Vallis, G. K., 2006: *Atmospheric and Oceanic Fluid Dynamics*. Cambridge University Press.
- Waite, M. L. and C. Snyder, 2009: The Mesoscale Kinetic Energy Spectrum of a Baroclinic Life Cycle. *J. Atmos. Sci.*, **66** (4), 883–901.